



pubs.acs.org/acsaom Forum Article

Developing Broadband Cr³⁺-Substituted Phosphor-Converted Near-Infrared Light Sources

Małgorzata Sójka, Jiyou Zhong, and Jakoah Brgoch*



Cite This: ACS Appl. Opt. Mater. 2023, 1, 1138–1149

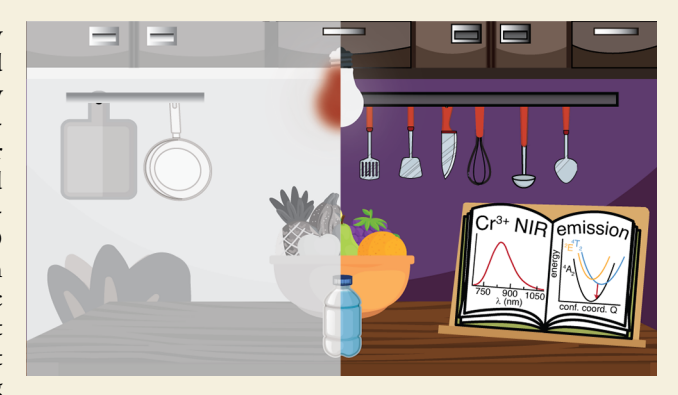


ACCESS |

Metrics & More

Article Recommendations

ABSTRACT: Near-infrared (NIR) spectroscopy is a rapidly growing research area due to its noninvasive, inexpensive, and rapid analysis capabilities spanning various applications. The key technology behind the growth of this field involves phosphorconverted NIR light-emitting diodes (pc-NIR LEDs) due to their energy efficiency, long operating lifetimes, and chemical and physical stability. Numerous studies have reported new Cr³+substituted phosphors that can more effectively convert blue LED emission to NIR radiation with a broad full-width-at-half-maximum (fwhm) that covers a significant portion of the interatomic vibrational spectrum. However, there is still much to learn about these materials' structure—property relationships. In this Spotlight on Applications, we discuss current research progress in designing



broadband Cr³⁺ phosphors as sources of NIR light, specifically emphasizing our research. We examine results from our work and others that have been used to create an efficient broadband emission in the NIR range. The discussion also emphasizes various techniques to analyze and improve temperature-dependent photoluminescence. Finally, we highlight the potential applications of Cr³⁺-based pc-NIR LEDs in fields such as night vision, bioimaging, and food freshness and analysis. This Spotlight on Applications aims to provide an overview of the progress of pc-NIR LEDs based on Cr³⁺ by emphasizing the challenges associated with its advancement while offering a few suggestions for ventures in this field.

KEYWORDS: pc-NIR LEDs, phosphors, Cr3+, broadband emission, luminescence

1. INTRODUCTION

Near-infrared (NIR) spectroscopy in the 700 nm to 1700 nm region of the electromagnetic spectrum has become a research hotspot due to its widespread application in medical diagnostics, night vision, has plant cultivation, has remote sensing, and food freshness analysis. The historical and universal approach for creating a NIR emission in this window has involved using tungsten lamps that produce a desirable broadband luminescence. However, these sources are extremely energy inefficient, with most energy lost as heat.9 By contrast, direct-emitter NIR light-emitting diodes (LEDs) based on epitaxial heterostructures of group III-V inorganic semiconductors such as InGaAlAs, InGaAs, or GaAs are highly energy efficient. 10 The drawback of this approach is that the LED emission has a narrow full-width half-maximum (fwhm < 50 nm), making it challenging to analyze the signal of multiple objects in different energy windows simultaneously. This can be overcome by implementing multiple NIR LEDs in a single device but at an increased device size, complexity, and cost. Unfortunately, LEDs also age at different rates, resulting in test discrepancies as the individual emission intensities of specific wavelengths diminish separately. In light of these challenges,

phosphor-converted NIR LEDs (pc-NIR LEDs) are currently considered the most promising solution due to their ability to cover most of the NIR region, low energy consumption, long operating lifetimes, and remarkable chemical and physical stability. Pc-NIR LEDs are a relatively new technology. It was only in 2016 when Osram released the first commercial pc-NIR LED, SFH4735. Since that time, tremendous progress has been made to improve these devices.

Pc-NIR LEDs operate by coating a blue-emitting InGaN LED chip with an inorganic phosphor that absorbs and down-converts the LED radiation to NIR photoluminescence. The primary research has focused on developing new phosphors that can more effectively convert the blue emission ($\lambda_{\rm em}=450$ nm) to the NIR. There are multiple strategies to achieve this down-conversion process. One approach implements the 4f \rightarrow

Special Issue: Phosphors for Infrared Applications

Received: February 14, 2023 Accepted: April 23, 2023 Published: May 4, 2023





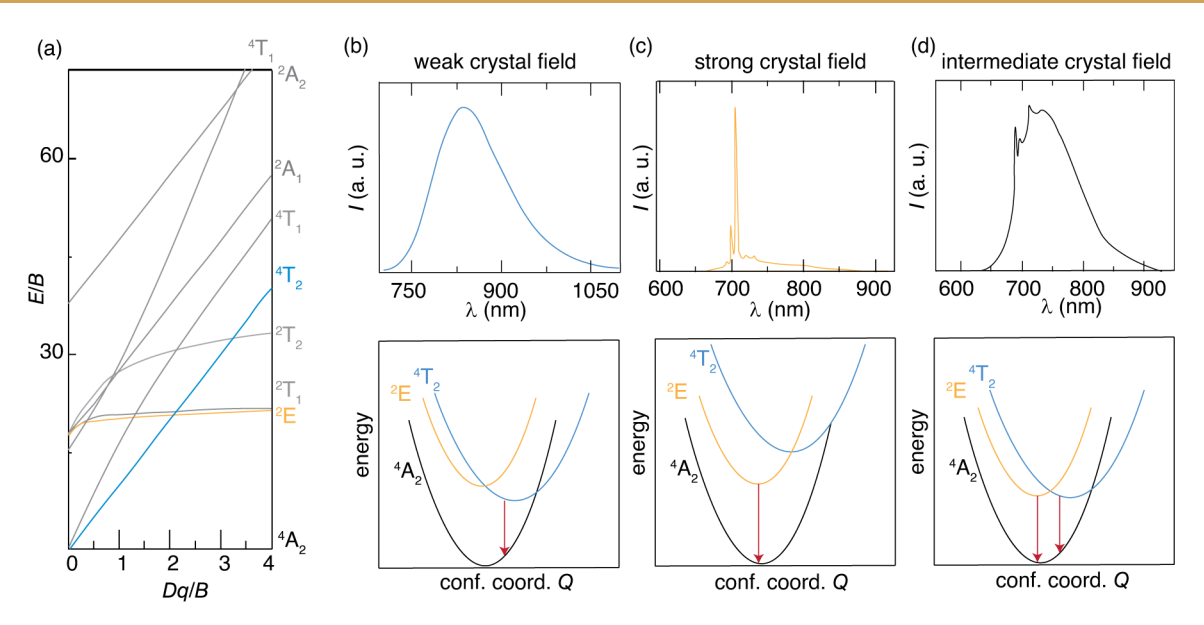


Figure 1. (a) The Tanabe-Sugano diagram for a d³ electronic configuration in an octahedral environment. The emission spectrum of Cr³⁺ and the respective configuration coordinate diagram under (b) weak, (c) strong, and (d) intermediate crystal field splitting.

4f luminescence of rare-earth ions such as Pr3+, Nd3+, Ho3+, Er3+, or Yb3+.12-16 Although reasonably practical, there are a few drawbacks to these systems. Most notably, the $4f \rightarrow 4f$ luminescence of the lanthanides is characterized by small values of fwhm, similar to direct-emitter materials. The $4f \rightarrow 4f$ electronic transitions are also forbidden, leading to weak blue light absorption.¹⁷ Additionally, many currently reported host lattices to have moderate phonon vibrational energies (>900 cm⁻¹) that can facilitate multiphonon relaxation, leading to quenching of the NIR luminescence, which impacts the photoluminescence quantum yield (PLQY).¹⁸ A method to overcome these limitations is to utilize luminescence from the spin-allowed, $5d \rightarrow 4f$ electronic transitions. However, it is tricky to design a phosphor that displays a rare-earths emission in the NIR range because such a low energy emission is most readily achieved by searching for phosphors with high crystal field splitting energy and low covalency. 19 To the best of our knowledge, there are no reports of Ce3+-substituted phosphors with an emission maximum beyond 750 nm. There are also only a few reports of NIR emission from Eu²⁺ that have been published. For example, the garnet-type Ca₃Sc₂Si₃O₁₂:Eu²⁺ phosphor covers the NIR range (700 nm-1050 nm), but the phosphor does not efficiently absorb blue light.²⁰ This incompatibility with commercial blue LEDs will hinder its commercial application in current blue-based pc-NIR LED devices. Another example that emits in the 600-900 nm range upon blue light excitation is K₃LuSi₂O₇:Eu²⁺, ²¹ while $Ba_{1+y}Sr_{1-y}Ga_4O_8:0.02Eu^{2+}$ (y = 0, 0.3, 0.5, 0.7) can be excited by blue light generating an emission centered at 670 nm to 775 nm depending on the Ba:Sr ratio.²² There are only a few Eu²⁺substituted phosphor systems reported to date, and much is left to learn about their structure-property relationships. 23,24 Beyond these rare-earth ions, transition-metal activators such as Bi³⁺, Mn²⁺, Ni²⁺, Mn⁴⁺, or Fe³⁺ have also been investigated, but most of these materials do not fulfill the optical property requirements for application. 25-28

Cr³⁺ is another ion studied for its optical properties and is of interest for NIR light production. Cr³⁺ has been a widely investigated activator ion since its success in the first ruby laser,

 α -Al₂O₃:Cr³⁺.²⁹ The ion's popularity stems from its tunable luminescence, excitation wavelength in the visible region, and high PLQY. The nature of the observed Cr3+ emission band strongly depends on the strength of the crystal field with a weak (octahedral) crystal field splitting environment resulting in broadband 3d \rightarrow 3d intraconfigurational spin-allowed ${}^{4}T_{2}$ → ⁴A₂ transitions. In contrast, strong crystal field splitting yields sharp line emissions from the spin-forbidden ${}^2{\rm E} \rightarrow {}^4{\rm T}_2$ transitions. The luminescence of Cr³⁺ can be deliberately tuned for specific applications by modifying the crystal field splitting energy to control the optical properties.³⁰ In the case of ruby, the strong crystal field experience by Cr^{3+} in α -Al₂O₃ results in a sharp, narrow emission centered in approximately the 690 nm to 720 nm range.²⁹ On the contrary, in a weak crystal field, broad NIR luminescence can be achieved with an fwhm between 130 nm to 340 nm ($\approx 1000 \text{ cm}^{-1}$ to 6000 cm⁻¹) depending on the number of crystallographic sites or any potential average and local structural distortions within the structure.³¹ These properties in tandem make Cr³⁺ the most promising activator for pc-NIR light sources where the ability to analyze multiple analytes reliably is imperative.

Over the past few years, our work and others have expanded the understanding of crystal chemistry in Cr3+-substituted phosphors by synthesizing and characterizing several novel materials with great potential for pc-NIR LED applications. 32-36 A number of reviews highlighting the fundamental spectroscopic characteristics of Cr³⁺, including the crucial role these compounds play in the context of NIR LEDs, are provided elsewhere. The goal of this Spotlight on Applications is to establish the fundamental structureproperty relationships enabling the design of these materials with an eye toward device integration. First, the basic spectroscopic properties of Cr3+ ions will be outlined. The crystal-chemical handles that yield efficient broadband NIR luminescence and thermally robust photoluminescence from Cr³⁺ investigated by our group and others will be discussed. Finally, the potential applications arising from using Cr³⁺ pc-NIR LEDs, from food freshness analysis to night vision, are highlighted.

2. SPECTROSCOPIC PROPERTIES OF THE Cr3+ ION

A profound understanding of the energy level structure and electronic transitions of Cr3+ is essential for the design of efficient, broadband NIR-emitting phosphors. When a luminescence center, or so-called activator ion, is incorporated within a host crystal structure, the ligands generate an electrostatic field that splits the 5-fold degenerate transition metal (TM) depending on the exact symmetry. When the central ion is inserted into an octahedral environment, the d orbitals split into the triply degenerate t_{2g} orbitals (d_{xy}, d_{xz}, d_{yz}) and the doubly degenerate, e_g orbitals $(d_{x^2-y^2}, d_{z^2})^{.39,40}$ Depending on the ligands, the energetic position of the t_{2g} and, e_g orbitals vary. In some cases of O_h symmetry, the d_{x-y}^2 and d_z^2 orbitals (e_g) experience greater repulsion relative to the triple-degenerate t_{2g} orbitals, which causes e_g to shift to higher energy and t_{2g} to fall energetically lower than e_g . In the case of tetrahedral symmetry, the effect is reversed, where the t_{2g} orbitals lie beneath the $e_{\rm g}$ orbitals in energy. The energy difference between $t_{\rm 2g}$ and $e_{\rm g}$ levels is expressed as $D_{\rm q}$, where $D_{\rm q}$ characterizes the strength of the crystal field splitting. D_q is described by eq 1, where z is the charge of the anion, e is the charge of an electron, r is the radius of the wave function, and R is the distance between the central ion and its surrounding ligands.

$$D_{\rm q} = \frac{ze^2r^4}{6R^5} \tag{1}$$

It is clear from eq 1 that the crystal field splitting energy is inversely proportional to the metal—ligand bond distance. As a result, a blue-shifted luminescence can be obtained by decreasing the metal—ligand bond distances and inducing stronger crystal field splitting.

2.1. Tanabe-Sugano Diagram for Cr³⁺

Fundamental knowledge about the optical properties of transition metals substituted in the inorganic host crystal structure can be well explained by Tanabe-Sugano diagrams. Figure 1a presents the Tanabe-Sugano diagram for transition metals with d^3 configuration with O_h symmetry, such as octahedrally coordinated Cr^{3+} . In Figure 1a, the x and y axes represent the D_q/B and E/B values, respectively, whereas E stands for the energy of the transition, and B is the Racah parameter, which describes exchange interactions between pairs of electrons and Coulomb repulsion. A decrease in B indicates smaller electron repulsion relative to the free TM ion, which implies that the d-orbital electron cloud is more extensive in the Cr3+-substituted material. This is well-known as the nephelauxetic effect. The reduction of the Racah parameter from its free ion value is defined as the nephelauxetic parameter β and can be calculated following eq 2:

$$\beta = \frac{B_{\text{complex}}}{B_{\text{free ion}}} \tag{2}$$

The size of the nephelauxetic effect depends on the bond strength between metal and ligand. Therefore, smaller β values indicate stronger covalency between the metal and ligand. In the case of ${\rm Cr}^{3+}$ materials, covalency and the local activator environment are essential to the tunability of the observed luminescence.

Three principal cases should be considered when analyzing the Tanabe-Sugano diagram for Cr³⁺. The first involves a weak

crystal field environment, where values of D_a/B are <2.3. As illustrated in Figure 1b, when $D_q/B < 2.3$, relaxation from the first excited state ⁴T₂ to the ⁴A₂ ground state results in a spinallowed radiative relaxation with a decay time of \approx 100 μ s. This broadband emission is desirable for application in pc-NIR LEDs because these transitions should cover the entire NIR region of interest (700 nm -1300 nm).⁴⁰ The fwhm and emission maximum can also be easily tuned due to the presence of multiple substitution sites or through crystal site engineering by creating solid solutions. This is further discussed in section 3.2. Conversely, in a strong crystal field environment, the value of $D_q/B > 2.3$, and the luminescence is characterized by narrow lines, typically in the deep red region of the visible spectrum, as presented in Figure 1c. The Tanabe-Sugano diagram reveals that the ²E state becomes the lowest excited level, and consequently the ²E \rightarrow ⁴A₂ transition is observed. Since this transition is forbidden not only by parity (Laporte rule) but also by the spin rule ($\Delta S = 0$), the luminescence spectrum resembles narrow $4f \rightarrow 4f$ transitions, and the radiative decay time is even longer than the luminescence originating from the 4T2 state, on the order of a few microseconds.

As illustrated in Figure 1d, the intermediate values when D_0 $B \approx 2.3$ lead to an intersection of the ${}^{4}T_{2}$ and ${}^{2}E$ levels at the minimum of the potential energy surfaces, which results in orbital mixing. As a result, the ion experiences strong and weak crystal fields simultaneously, enabling radiative relaxation from two excited states. The outcome is a combination of narrow emission lines overlapping with the broadband emission. These systems are desirable for luminescence thermometry because an increase in temperature induces a thermal population to a higher energy excited state. 6,41,42 This causes a drastic change in peak shape from sharp line emission to broadband emission. However, for pc-NIR LEDs, this phenomenon is not favorable since the emission band's shape, position, and fwhm should remain thermally stable up to 423 K, which is the temperature that LEDs can reach during operation. Therefore, ideally, there should be a lack of coupling between ²E and ⁴T₂ excited states at elevated temperatures.

3. DESIGN RULES FOR THERMALLY ROBUST, EFFICIENT, AND BROADBAND Cr³⁺-SUBSTITUTED PHOSPHORS

The observed luminescence from Cr³+ depends upon the Racah parameter or the crystal field splitting energy. Therefore, targeting an appropriate covalency and crystal field environment is essential for designing next-generation NIR-emitting phosphors. Sadly, it is not enough to simply produce a broadband NIR emission. The phosphor must have a sufficiently broad fwhm to cover the NIR region of interest, whether biological windows I and II or the region to assess food freshness (800 nm−1350 nm). The materials must also have a high quantum efficiency under blue light excitation. Therefore, our work and others have focused on establishing new strategies for enhancing the luminescent properties of Cr³+-substituted phosphors that can be assembled into design guidelines to address each of these requirements.

3.1. Multisite Occupancy for Broadband Photoluminescence

One universal strategy for obtaining broadband luminescence is to target inorganic host crystal structures with more than one crystallographic site for Cr^{3+} substitution. Indeed, structures

ACS Applied Optical Materials

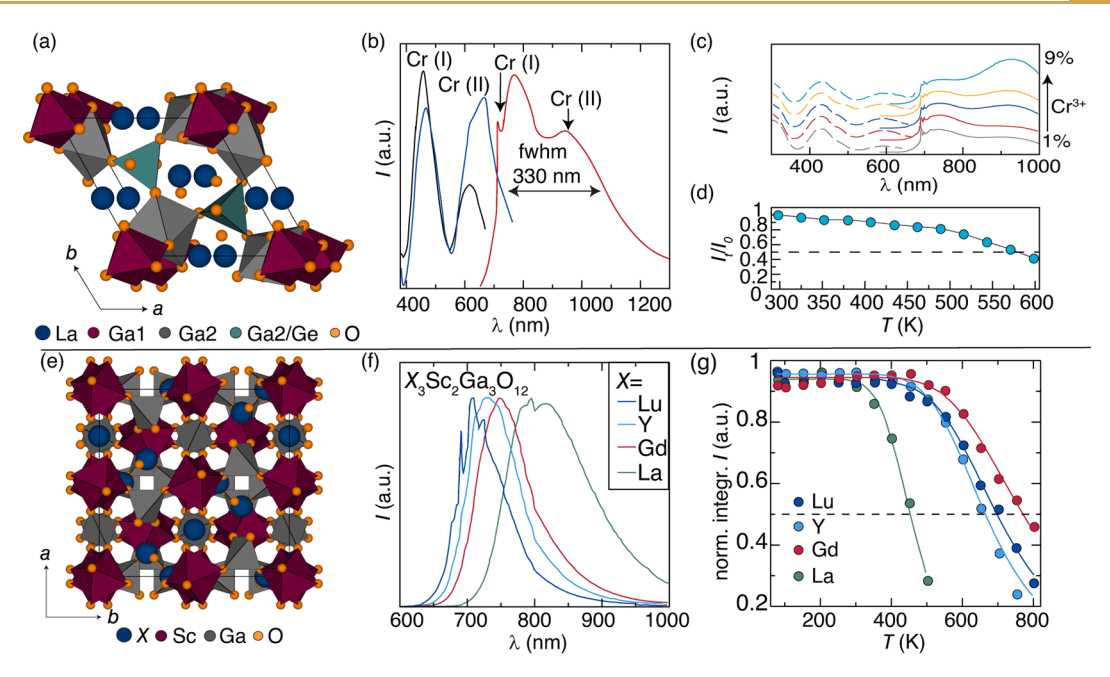


Figure 2. (a) The crystal structure of La₃Ga₅GeO₁₄ is drawn to highlight the $[Ge/GaO_4]$ tetrahedra (green) and two independent $[GaO_6]$ octahedral units (red and gray). (b) The excitation ($\lambda_{em,I} = 700$ nm, $\lambda_{em,II} = 850$ nm) and emission spectrum ($\lambda_{ex} = 473$ nm) of La₃Ga₅GeO₁₄:0.05Cr³⁺ were recorded at room temperature. (c) The photoluminescence excitation (dashed) and emission (solid) spectra of La₃Ga₅GeO₁₄:xCr³⁺ where x = 1% (gray), 3% (red), 5% (navy), 7% (yellow), and 9% (blue). (d) The thermal stability of La₃Ga₅GeO₁₄:xCr³⁺ phosphor was investigated through temperature-dependent luminescence measurements. (e) The crystal structure of XSc₂Ga₃O₁₂ where X = Lu, Y, YGd, and YGd, YGd, and YGd, YGd, and YGd, YGd, and YGd, and YGd, YGd, YGd, and an emission YGd, and

with multiple crystallographically independent polyhedral environments with different geometries, bond lengths, and polyhedral volumes produce different magnitudes of crystal field splitting, increasing the emission fwhm. This multisite strategy has been successfully used to obtain a vast emission band (fwhm = 330 nm or $\approx 6100 \text{ cm}^{-1}$) in La₃Ga₅GeO₁₄:Cr³⁺. This host crystal structure has three independent sites capable of accommodating Cr3+, two GaO6 octahedra, and one disordered (Ga/GeO₄) tetrahedron (Figure 2a). The latter is occupied in a 1:1 ratio of Ge⁴⁺ to Ga3+. X-ray absorption near-edge structure (XANES) and electron paramagnetic resonance (EPR) measurements revealed that the Cr³⁺ simultaneously occupies the octahedral and tetrahedral sites. This leads to the broad emission band that can be excited by blue light ($\lambda_{ex} = 450 \text{ nm}$), as shown in Figure 2b. The emission spectrum spans 650 nm-1200 nm with two distinct maxima at \approx 800 nm and 980 nm, originating from Cr³⁺ in octahedral and tetrahedral positions, respectively. Increasing the Cr3+ concentration does not influence the excitation spectra (Figure 2c), although the emission intensity of the peak located at 950 nm increases. This phenomenon was also observed in the BaMgAl₁₀O₁₇:Cr³⁺ phosphor, where the fwhm was increased 10-fold by site-selective occupation. 43 As the concentration of Cr3+ increases, the activator occupies both octahedral [AlO₆] crystallographic sites in the host, resulting in an fwhm = 92.6 nm ($\approx 2000 \text{ cm}^{-1}$). Nevertheless, the fwhm of this emission band is not quite wide enough to meet the requirements of pc-NIR LED lighting because the emission maximum occurs at relatively high energy λ_{em} = 690 nm. Broadband emission was also achieved in the La₂MgZrO₆:Cr³⁺ phosphor with an outstanding fwhm of 210 nm ($\approx 3190 \text{ cm}^{-1}$) due to the presence of Cr3+ on the ZrO6, and MgO6 distorted octahedral sites. 44 The substitution of an activator ion on more

than one crystallographic site is one viable method for designing broadband NIR-emitting phosphors that can be utilized in blue LED-based NIR spectroscopy.

3.2. Modulating Crystal Field Splitting To Tune the

Broadband NIR-emitting phosphors can also be developed by tuning the emission maximum. One of the most common approaches for red-shifting the emission maximum is modifying the local coordination of Cr^{3+} since D_q strongly depends on the cation-ligand distance (eq 1). Studies based on varying covalency in the $X_3Sc_2Ga_3O_{12}$ garnet family (X = Lu, Y, Gd, La) have shown that the position of the Cr3+ emission band can be tuned from 690 to 810 nm. 45 Garnets crystallize in cubic space group $Ia\overline{3}d$ with the chemical formula $A_3B_5O_{12}$ or $A_3B_2C_3O_{12}$, where A, B, and C represent different cations. Figure 2e illustrates the crystal structure containing three crystallographically independent sites for Cr3+ substitution. It is expected that Cr^{3+} $(r_{6-coord} = 0.615 \text{ Å})^{46}$ would substitute on the octahedral [ScO₆] site ($r_{6\text{-coord}} = 0.745 \text{ Å}$) rather than the $[GaO_4]$ tetrahedral position ($r_{4\text{-coord}} = 0.390$ Å). Analyzing Figure 2f, the emission spectrum of Lu₃Sc₂Ga₃O₁₂:Cr³⁺ (dark blue) consists of superimposed transitions from the ${}^4\mathrm{T}_2$ and ${}^2\mathrm{E}$ levels to the ground state of the Cr^{3+} . Replacing Lu^{3+} with ions of progressively larger ionic radii $(Lu^{3+} < Y^{3+} < Gd^{3+} < La^{3+})$ leads to the linear increase of the lattice parameters and, consequently, an increase in the Cr3+-O2- distance. As a result, the crystal field strength decreases, as observed in the luminescence spectra, where a significant red shift occurs from $X = Lu^{3+}$ to $X = La^{3+}$ by almost 120 nm. The calculated D_q/B values decrease from 2.57 to 2.27, proving the smaller crystal field splitting and conseqa lack of luminescence from the ²E excited state. Regardless, these garnet materials do not possess a wide enough emission fwhm

ACS Applied Optical Materials

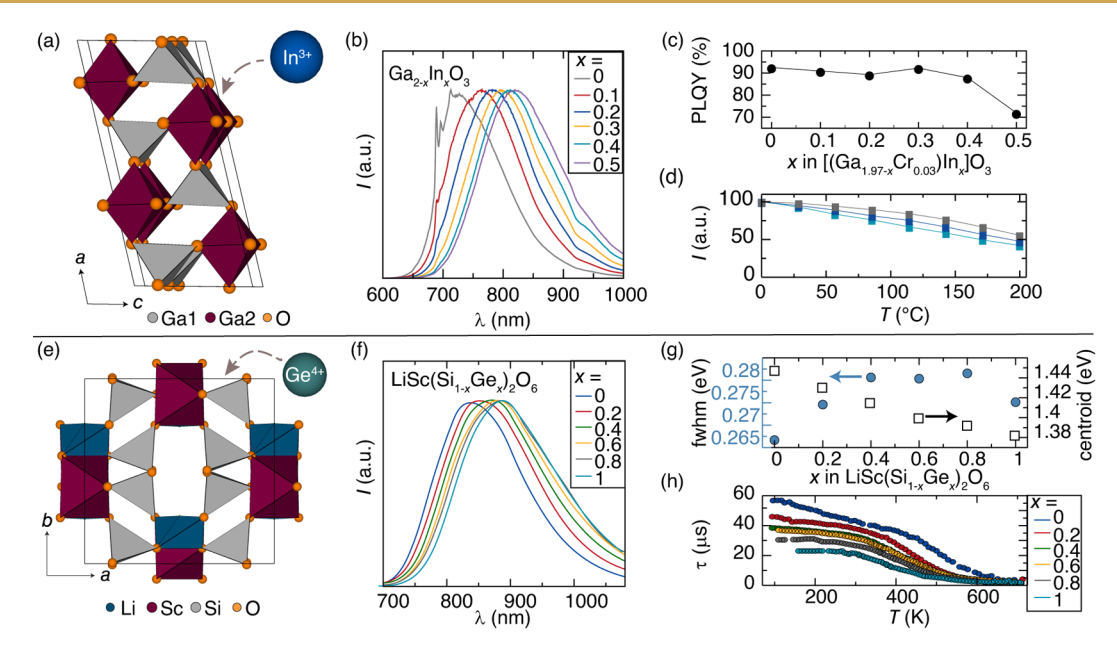


Figure 3. (a) The crystal structure of β-Ga₂O₃. As proven by density functional theory techniques, the substitution of In^{3+} for Ga^{3+} occurs on the octahedral sites exclusively. (b) The luminescence spectra of $Ga_{2-x}In_xO_3$: Cr^{3+} with a different In^{3+} concentration were recorded at $λ_{ex} = 450$ nm. (c) Photoluminescence quantum yield of $Ga_{2-x}In_xO_3$: Cr^{3+} as a function of x concentration. (d) Temperature-dependent integrated emission areas of $Ga_{2-x}In_xO_3$: Cr^{3+} phosphors where x = 0, 0.2. 0.4. (e) Crystal structure of $LiScSi_2O_6$. Ge^{4+} ions likely replace Si^{4+} , forming tetrahedrons. (f) Luminescence spectra of $LiSc(Si_{1-x}Ge_x)_2O_6$: Cr^{3+} for the full Ge:Si range. (g) fwhm and centroid as a function of $Ge:Si^{2+}$ concentration. (h) Temperature-dependent decay time of the $LiSc(Si_{1-x}Ge_x)_2O_6$: Cr^{3+} solid solution. Panels b-d: modified from ref 33. Panels f-h modified from ref 47.

for NIR application; however, it is evident that cation substitution is an effective strategy to red-shift the emission maximum toward NIR emission.

The surrounding coordination environment of the activator ion can also be influenced by creating a solid solution. Indeed, intentionally introducing structural distortions can cause desirable inhomogeneous broadening of the emission band. As recently presented by our work, the luminescent properties of β -Ga₂O₃:Cr³⁺ can be nicely tuned by substituting Ga³⁺ with In³⁺³³ The crystal structure of β -Ga₂O₃ belongs to the monoclinic C2/m (no. 12) space group. As shown in Figure 3a, the structure comprises distorted [GaO₆] octahedral units corner-connected with [GaO₄] tetrahedra to produce a threedimensional network. Rietveld refinement and formation energy calculations agree that both In³⁺ and Cr³⁺ preferentially substitute on the octahedral sites over the tetrahedral sites. The luminescence of Cr^{3+} can be excited by blue ($\lambda = 450 \text{ nm}$) light, leading to a broad luminescence covering the 600 nm -1000 nm spectral region (Figure 3b). Substitution of In³⁺ by Ga^{3+} induces weaker crystal field splitting, and D_q/B decreases from 2.65 in $[(Ga_{1.97}Cr_{0.03})]O_3$ to 2.37 in $[(Ga_{1.47}Cr_{0.03})In_{0.5}]$ -O₃. Consequently, the emission peak maximum shifts toward longer wavelengths from ~713 nm to 820 nm, and the fwhm also increases from 122 nm to 157 nm. These changes stem from modulating the crystal field splitting energy through In³⁺ substitution, which distorts the crystal structures and broadens the emission band. Most importantly, the photoluminescence quantum yield remains nearly constant as a function of In³⁺ substitution, between 85% and 90%, until x = 0.5, where the PLQY decreases to 72%. For samples containing x = 0, 0.2, and 0.4, the luminescence intensity signal remains high even at elevated temperatures with 77% for x = 0, which decreases to 60% compared to the room temperature emission intensity when x = 0.40 (see Figure 3d).

Finally, Van Bunningen et al. investigated the luminescent properties of a $LiSc(Si_{1-x}Ge_x)_2O_6$ clinopyroxene solid solution substituted with Cr^{3+} 47 $LiScSi_2O_6$ crystallizes in monoclinic space group C2/c (no. 15) and is isostructural with LiScGe₂O₆, allowing for the creation of a complete solid solution by varying the ratio between Si:Ge. Figure 3e presents the structure of the investigated material. It consists of alternating tetrahedrally coordinated Li⁺ and Si⁴⁺ layers along with octahedral [ScO₆] units. Due to their similar ionic radii and charge, Ge⁴⁺ replaces Si⁴⁺ ions, while Cr³⁺ most likely occupies the octahedrally coordinated [ScO₆] polyhedron. The material can be excited by blue radiation (λ_{ex} = 450 nm) to produce a broad emission band covering the NIR range of the spectrum. As plotted in Figure 3f,g, the $\lambda_{\rm em}$ shifts with increasing Ge content in the investigated materials by around 645 cm⁻¹. As revealed in Figure 3g, a distortion in the second coordination sphere in the Ge4+:Si4+ results in an inhomogeneous broadening of the emission band, with the broadest fwhm observed in the mixed Ge:Si system (fwhm = 2258 cm⁻¹ for α = 0.8). An analogous approach was utilized in (LiIn)_{1-v}Zn_{2v}InSbO₆.³ Considering coordination number, as well as the ionic radii of Zn2+, a cosubstitution of Zn2+ onto the Li+ and In³⁺ site occurs. Consequently, the cosubstitution causes a contraction of the In-O bonds and increases the D_a/B values, inducing a blue-shift in the luminescence. The emission peak shifts from 965 nm to 892 nm, and the biggest fwhm was 235 nm (2452 cm^{-1}) for $(\text{LiIn})_{0.8}\text{Zn}_{0.4}\text{InSbO}_6:\text{Cr}^{3+}$.

3.3. Temperature-Dependent Considerations for Cr³⁺ Phosphors

Beyond possessing a broadband emission, other requirements must be fulfilled when designing efficient Cr³⁺ phosphors for NIR pc-LEDs, such as high PLQY of the material expressed as a ratio between the number of emitted photons relative to the

Table 1. Summary of Select Cr^{3+} -Substituted Phosphors with the Reported D_q/B , fwhm, S, PLQY, $I_{423 \text{ K}}$ Values, Excitation, And Maximum Emission Wavelength

formula	$D_{\rm q}/B$	$\lambda_{\rm ex} \ (\rm nm)$	λ_{em} (nm)	fwhm	PLQY (%)	S	$I_{423 \text{ K}}$ (%)	ref
Weak Crystal Field								
NaGaP ₂ O ₇ :Cr ³⁺	1.98	460	793	$1780 \text{ cm}^{-1}/115 \text{ nm}$	56.4	2.26	85.5	52
K ₂ NaScF ₆ :Cr ³⁺	2.06	450	765	$1709 \text{ cm}^{-1}/101 \text{ nm}$	74.0	2.96	89.6	53
GaTaO ₄ :Cr ³⁺	2.29	460	840	$1872 \text{ cm}^{-1}/140 \text{ nm}$	91.0	3.82	60	35
$Gd_{3}Sc_{1.42}Ga_{0.5}Ga_{3}O_{12}$: Cr^{3+}	2.45	460	756	$1682 \text{ cm}^{-1}/120 \text{ nm}$	91.0	-	86	54
$KAlP_2O_7:Cr^{3+}$	1.90	450	790	$1852 \text{ cm}^{-1}/120 \text{ nm}$	78.9	2.58	77	55
K ₂ NaInF ₆ :Cr ³⁺	1.79	450	774	$1855 \text{ cm}^{-1}/124 \text{ nm}$	70.2	2.52	78.3	56
LaTiTaO ₆ :Cr ³⁺	2.12	354	950	$3184 \text{ cm}^{-1}/300 \text{ nm}$	10.23	9.19	24.64	51
Y ₃ In ₂ Ga ₃ O ₁₂ :Cr ³⁺	2.24	450	760	$1567 \text{ cm}^{-1}/125 \text{ nm}$	91.60	1.60	100	50
Gd ₃ Al ₂ Ga ₃ O ₁₂ :Cr ³⁺	-	445	730	$1562 \text{ cm}^{-1}/70 \text{ nm}$	97.3	-	96.8	57
GdAl ₃ (BO ₃) ₄ :Cr ³⁺	2.48	420	740	$1678 \text{ cm}^{-1}/140 \text{ nm}$	91	-	100	58
SrAl ₆ Ga ₆ O ₁₉ :Cr ³⁺	≈ 2.5	450	770	$\approx 1719 \text{ cm}^{-1}/110 \text{ nm}$	84	-	≈100	59
Intermediate/Strong Crystal I	Field							
$Sr_3Sc_4O_9$: Cr^{3+}	2.69	468	761	$1721~{\rm cm}^{-1}/120~{\rm nm}$	87.00	2.58	≈ 45	60
BaMgAl ₁₉ O ₁₇ :Cr ³⁺	2.52	399	692	$2000 \text{ cm}^{-1}/92 \text{ nm}$	94.00	-	63.00	43
$Y_2CaAl_4SiO_{12}:Cr^{3+}$	2.62	440	750	$2293 \text{ cm}^{-1}/160 \text{ nm}$	-	-	-	61
$SrGa_{12}O_{19}$: Cr^{3+}	3.42	448	750	$1625 \text{ cm}^{-1}/78 \text{ nm}$	96.55	-	80.00	62
α -Al ₂ O ₃ :Cr ³⁺	2.81	405	695	-	87.1	-	48.2	4
LaGaO ₃ :Cr ³⁺	2.87	450	727	-	-	-	-	63
ZnAl ₂ O ₄ :Cr ³⁺	3.68	384	687	-	-	-	-	64

absorbed photons. The PLQY can be correlated with the rate of the radiative $(k_{\rm R})$ and nonradiative $(k_{\rm NR})$ transitions as presented in eq 3:

$$\Phi(1) = \frac{k_{\rm R}}{k_{\rm R} + k_{\rm NR}} \tag{3}$$

Radiative de-excitation pathways lead to the generation of photon emission, where nonradiative pathways are associated with the liberation of vibrational energy. To much extent, the temperature-dependent changes in luminescence intensity originate from the fluctuations of the nonradiative transition rate probability. Consequently, increasing the probability of nonradiative transitions will directly decrease the PLQY. Bearing in mind that current InGaN LEDs operate at ~423 K, phosphors are only considered thermally robust if they have a minimum T_{50} (defined as the temperature at which the intensity/decay time of the luminescence is 2-fold lower than at the lowest temperature) above 423 K. 48 For example, temperature-dependent luminescence measurements on La₃Ga₅GeO₁₄:Cr³⁺ were conducted to investigate the thermal stability of the phosphor.³¹ The phosphor possesses a high T_{50} of ≈560 K, which is sufficient for application in a NIR pc-LED (Figure 2d). Yet, it is unclear what changes in the crystal chemistry suggest further work to establish the mechanisms of thermal quenching in these phosphors.

As noted, it is essential to account for the change in optical properties as a function of temperature. The correlation between the intensity of the luminescence and temperature can be expressed by using eq 4:¹⁹

$$I(T) = \frac{I_0}{1 + \frac{\Gamma_0}{\Gamma_0} \exp\left(-\frac{\Delta E}{k_B T}\right)}$$
(4)

where Γ_0 is the radiative lifetime at 0 K (in practice when no thermal quenching occurs), $\Gamma_{\rm v}$ corresponds to the attempt rate of nonradiative transitions, $k_{\rm B}$ is a Boltzmann constant, and ΔE is the activation energy responsible for the quenching process. The value of ΔE can be easily obtained by fitting the integrated

emission intensity or the photoluminescent lifetime as a function of temperature. Usually, a small value of ΔE indicates a high probability of quenching processes within the investigated material, whereas a large ΔE indicates better thermal stability. There are two main pathways responsible for the quenching processes in the phosphors. The first one involves a thermally activated photoionization process. If the bandgap of the materials is not wide enough, the excited levels of Cr3+ can be near the conduction band. With increasing temperature, the thermally activated photoionization process becomes increasingly likely, as the excited electron and conduction band wave functions effectively couple, promoting photon extraction. Activation energy responsible for the quenching process (ΔE) corresponds to the distance between the bottom of the conduction band and the lowest energy excited 3d orbital. To prevent the photoionization process, it is essential to choose a host structure with a wide bandgap (E_g > 2). 17 The second mechanism is a thermally induced crossover process where a thermal quenching occurs at an intersection between the excited- and ground-state potential energy surfaces. Here, ΔE corresponds to the distance between the crossing point and the lowest vibrational level of the excited state. The equilibrium distance between the ground and excited parabola can be determined utilizing the Huang-Rhys parameter (S), which indicates the magnitude of the electron phonon coupling. One of the universal approaches for the determination of the Huang-Rhys parameter is fitting the temperature-dependent emission fwhm using eq 5, where $\hbar v$ is the phonon energy: 48

$$fwhm(T) = \sqrt{8 \ln 2} \times \hbar v \times \sqrt{S \, coth(\hbar v / 2k_B T)}$$
 (5)

A large value of S indicates stronger electron—phonon coupling, which leads to a broader emission bandwidth. However, unfortunately, it also facilitates the probability of nonradiative transitions due to the higher S value causing a more significant shift between the excited and ground potential energy surfaces, which increases the likelihood of an intersection point and leads to lower values of ΔE . The

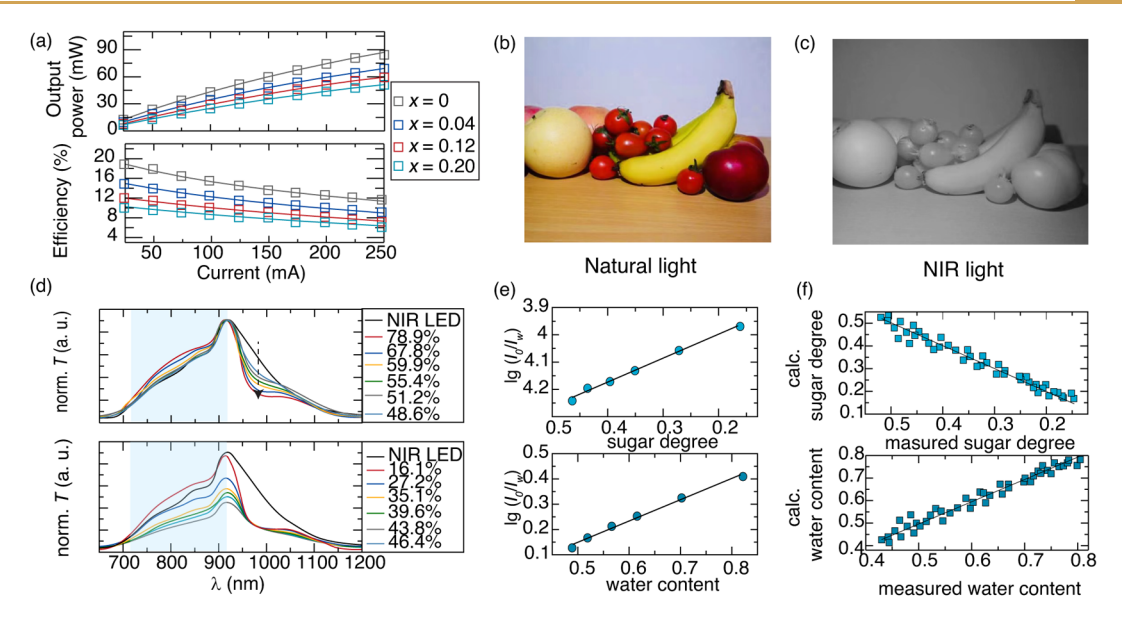


Figure 4. (a) NIR output power and photoelectric energy conversion efficiency of $Ga_{1.97-2x}Mg_xGe_xCr_{0.03}O_3$ (x=0, 0.04, 0.12, and 0.2) as a function of driving current. Photography of fruits taken by (b) natural light and (c) NIR camera. Reprinted with permission from ref 32. Copyright 2022 American Chemical Society. Normalized transmittance spectra of $Mg_3Ga_2GeO_8$: Cr^{3+} phosphors after penetrating a pear with different (d) water contents and (e) sugar contents. A linear relationship between absorbance and (f) sugar degree or (g) water content. Measured versus calculated (h) sugar content or (i) water content. Panels a-c modified from ref 32. Panels d-i modified from ref 69.

crossover process is also observed in the garnet phosphors, as discussed above and plotted in Figure 2g. The thermal stability decreased from Lu₃Sc₂Ga₃O₁₂:Cr³⁺ ($T_{50} = 710$ K) to La₃Sc₂Ga₃O₁₂:Cr³⁺ ($T_{50} = 410$ K).⁴⁵ This is probably due to stronger electron—phonon coupling and the lower energy of the excited Cr³⁺ orbitals, which leads to a crossover point between the ground and excited potential energy surfaces.

Generally, the poor T_{50} hinders the applicability of this material in pc-NIR LEDs and needs to be improved. Similarly, in the example of LiSc($Si_{1-x}Ge_x$)₂O₆, expanding the fwhm and maximum of the emission band by substituting Si for Ge as desired naturally causes the T_{50} to decrease following an increase in S (eq 4) with the thermal quenching dropping from 539 to 393 K, as plotted in Figure 3h.⁴⁷ One method to minimize nonradiative relaxation through the crossover process and increase the PLQY is to ensure that the host crystal structure is rigid. However, the distinction of host lattices that possess greater structural rigidity than others by merely comparing their crystal structures can often be challenging. One of the ways to determine structural rigidity is to calculate a material's Debye temperature $(\Theta_D)^{49}$. This can be done by using density functional theory (DFT) calculations. As shown in Y₃In₂Ga₃O₁₂:Cr³⁺ material, Debye temperature reaches 599 K.50 Consistently, calculated PLQY reaches an impressive 91% value. Therefore, combining a wide energy gap and $\Theta_{\rm D}$ can serve as a proxy for a phosphor's PLQY and be used to screen inorganic crystal structure databases.

3.4. Cr³⁺ Phosphors of Interest in the Literature

The optical properties of Cr^{3+} -substituted phosphors in select host crystal structures are presented in Table 1, along with their D_q/B values, Huang—Rhys parameter (S), PLQY, and I_{423} . The strong dependence of Cr^{3+} on crystal field splitting and the nephelauxetic effect dramatically influence the exploration of new broadband NIR-emitting phosphors. Based on observations from the literature, the covalency between Cr^{3+} and the ligand cannot exhibit values of D_q/B that

are too low or too high or, consequently, stronger crystal field splitting will result. This will cause radiative relaxation exclusively from the ²E excited level. For example, the LaGaO₃:Cr³⁺ perovskite phosphor (see Table 1) has a D_0/B value of 2.87, producing a luminescence spectrum composed only of narrow lines. Instead of focusing on strongly covalent host structures such as LaGaO₃ or α -Al₂O₃, research should focus on more ionic hosts, which tend to produce broadband luminescence originating from the 4T2 excited level. Thus, fluorides, phosphates, and some garnets, as presented in Table 1, are of interest. Besides covalency, electron-phonon coupling also plays a crucial role in evaluating the applicability of the Cr³⁺ phosphors in NIR LEDs. As shown in LaTiTaO₆:Cr³⁺ phosphor, despite an impressive broad fwhm (\sim 300 nm/3184 cm⁻¹), the estimated S parameter reaches 9.19, resulting in a poor PLQY value (10.23%) and low $I_{\rm 423~K}$ (24.64%). Conversely, an extraordinary $I_{423 \text{ K}}$ (100%) was reported in Y₃In₂Ga₃O₁₂:Cr³⁺ phosphors with a high PLQY (\sim 91.60%). This can be attributed to the relatively low S parameter value of only 1.60.50

It is important to note that the materials presented in Table 1 are among the only weak crystal field systems with all of these parameters reported. Researchers investigating Cr³+substituted phosphors often omit many of these vital parameters in their reports, limiting a complete understanding of the material's optical properties and their applicability in pcNIR LED devices. As valuable as these reports on phosphors are, the field can be even further improved by performing a complete analysis of a material, which includes investigating the Huang—Rhys parameter. This can give insight into the factors that control a phosphor's fwhm and thermal stability, enabling the development of highly efficient phosphors. Moreover, if future researchers want to apply machine learning to identify promising materials more rapidly, then access to this data is vital for building a reliable training set.

ACS Applied Optical Materials

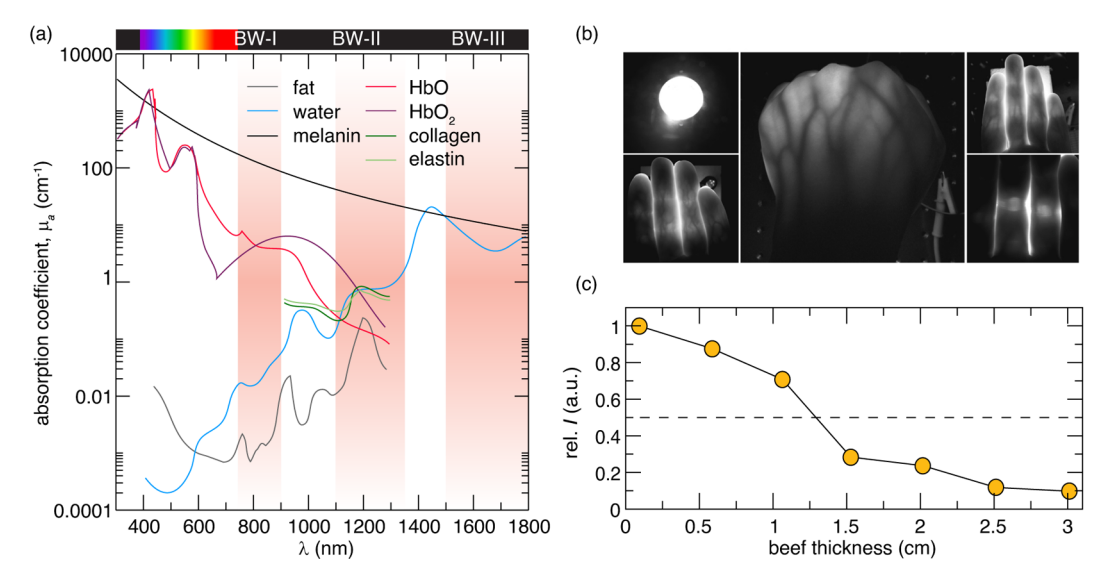


Figure 5. (a) Extinction spectra of tissue components responsible for increased imaging depth correspond to the different biological windows (BW-I, BW-II, and BW-III) where light can penetrate deeper along with better contrast of the emission. (b) Images of vessels taken by using a Cr³⁺-substituted NIR-LED device. Reprinted with permission from ref 70. Copyright 2022, American Chemical Society. (c) Penetration of NIR light through beef with different thicknesses. Modified from ref 71.

4. APPLICATIONS OF NIR PC-LEDS BASED ON Cr3+

The success of pc-NIR LEDs depends on two factors: fwhm of the band and radiant flux. For simultaneous detection of vibrational modes of different functional groups, it is necessary to have a broad fwhm that covers as much of the NIR region as possible. This is how these light sources can enable efficient and noninvasive sensing of indigents such as water, fats, proteins, or the presence of pesticides, as each has a characteristic fingerprint in a given spectral range. The radiant flux, defined as the amount of radiant energy that emerges from a source per unit of time, is also essential. The relationship between radiant flux (also known as light output) and current in LED chips can be complex and depends on several factors. However, in general, the radiant flux of an LED increases with increasing current up to a certain point, after which the radiant flux decreases. This behavior is because the efficiency of LED (light output/power input) decreases due to the heating of the material, which can facilitate nonradiative transitions. A similar quenching process occurs in the phosphor coating. Therefore, optimizing the operating current to maximize radiant flux is essential. The ideal performance of pc-NIR LEDs should reveal simultaneously high output power with a relatively low input current, which is related to the phosphor material's efficiency and also a broad light distribution.

4.1. Night Vision

Night vision has been employed across industries, addressing the needs of military and rescue activities, security, engineering, and medical applications. The most common NIR light sources used in night vision are tungsten and halogen lamps. As mentioned in the introduction, these light sources are highly inefficient due to the amount of heat they produce and their relatively short operating lifetimes. Thus, one of the promising solutions is applying Cr³⁺-substituted phosphors as more effective NIR light sources. The proposed strategy's potential has been nicely demonstrated in numerous scientific papers^{2,33,65-67} where researchers show the potential of these

systems by taking digital photographs of samples irradiated with a NIR pc-LED and detected using a NIR camera.

For example, our work investigated the potential usability of Cr^{3+} for night imaging in $Ga_{1.97-2x}Mg_xGe_xO_3$: Cr^{3+} , where x =0, 0.04, 0.12, and 0.2.32 Elemental substitution modified the crystal field splitting, which resulted in a tunable, red-shifted emission band as the Mg and Ge content increased. The device's performance was evaluated by coating the phosphor on a blue LED chip. As depicted in Figure 4a, NIR output power increases as a function of driving current without any visible saturation. However, the efficiency of the phosphor decreases along with the increment of current. The highest efficiency is achieved for Ga₂O₃:Cr³⁺ phosphor (43.4 mW@ 15.3%, driven by 100 mA). The practical application of fabricated NIR pc-LED was further demonstrated in Figure 4b,c. The results show that under NIR light produced by the prototype device, black-and-white fruit images are easily distinguishable, suggesting a potential for these materials in spectroscopic applications. Similar research was conducted in ScF₃:Cr³⁺ phosphors.⁶⁷ Due to the weak crystal field splitting, it was possible to observe the luminescence of Cr3+ in the 700-1100 nm range. However, the building prototype reveals relatively poor efficiency and radiant power (≈7.5 mW@2.65 driven by 100 mA). The effectiveness of the night vision application was also demonstrated in Ca₃Sc₂Si₃O₁₂:Cr³⁺ phosphor by capturing a digital photograph of water and milk using the fabricated device as the NIR light source.⁶⁸ The phosphor shows excellent performance as a fabricated highpower NIR LED device, with its optical power reaching nearly 110 mW at 520 mA while showing no signs of saturation.

4.2. Food Analysis

The capability of pc-NIR LEDs for food analysis was investigated using the ${\rm Mg_3Ga_2GeO_8:Cr^{3^+}}$ phosphor to determine water content and sugar degree in fruit. ⁶⁹ It was possible due to the overlapping of the emission spectra of ${\rm Cr^{3^+}}$ with second overtones of the O–H stretching band (970 nm–980 nm) and third (~910 nm) and fourth (~750 nm) overtones of C–H stretching vibrations in soluble sugars such

as fructose, glucose, or sucrose. The NIR light penetrated the pears in the experiment with different water and sugar contents. A significant drop in the transmission spectra at ~980 nm occurs following the increasing water content (Figure 4d). This is due to water reabsorption. Analogously, Figure 4e shows that increasing the amount of sugar led to a decrease intensity in the 720 nm-910 nm range. As depicted in Figure 4f,g, a comparison of the actual water and sugar contents derived from the experiment results in an excellent linear correlation. Therefore, using Lambert-Beers law, it was possible to calculate an experimental water and sugar content, and as presented in Figure 4h,i, there is a good agreement between actual and determined content. As shown by our work, Cr3+ phosphors can also be effectively utilized for analyzing food freshness by capturing tissue damage of the fruit using an NIR camera, which is not visible to the naked eye.³³ The examples highlighted here demonstrate that a nondestructive method for food quality can be achieved by using broadband phosphor as an NIR light source. It is also important to note that applying Cr3+-substituted phosphors in food quality analysis is a relatively new field, and discoveries, applications, and successes will be made as research in this area continues.

4.3. In Vitro Imaging

The use of NIR radiation is a paramount requirement for tissue imaging. The absorption of different components such as melanin, fat, water, or hemoglobin has a particular spectral window, as plotted in Figure 5a, that falls into three distinct biological windows: 650 nm 950 nm (I), 1000 nm–1350 nm (II), and 1550 nm–1870 nm (III). Irradiating samples using one of these windows enables light to penetrate tissues up to a few centimeters. Unfortunately, under oxidizing conditions, Cr^{3+} can coexist with Cr^{4+} and Cr^{6+} , increasing chromium toxicity and limiting its usability as an in vivo marker. Regardless, it is still possible to use Cr^{3+} for in vitro imaging.

For example, K₂NaGaF₆:Cr³⁺ phosphor was investigated with applications aimed at venography⁷⁰ Bearing in mind that hemoglobin in the blood can absorb some NIR photons when NIR light passes through tissue cells, it is possible to clearly distinguish blood vessels that absorb the photons compared to the joints in the fingers and palm that absorb less by changes in brightness and darkness in the recorded image, as shown in Figure 5b. An analogous case was presented in the isostructural K₂NaInF₆:Cr³⁺ phosphor, where the NIR radiation penetrated the wrist about 4 cm with a well-resolved image of the distribution of veins.⁵⁶ The influence of the thickness of beef on the NIR depth penetration was investigated by using the NIR radiation in ScBO₃:Cr³⁺ phosphor.⁷¹ The results revealed that the tissues could be effectively penetrated even at 1 cm, where only 30% of the initial luminescence intensity is lost after passing through the beef (see Figure 5c). Above 1 cm, only ≈25% of the initial emission intensity passes through the beef. An exciting example of dental analysis using NIR spectroscopy was presented by the Sr₉Sc(PO₄)₇:Cr³⁺ phosphor. 72 The authors described constructing an NIR device for dental imaging analysis. On the basis of the captured NIR images, it was possible to judge the tooth calcification compared with visible measurement. This approach would open an opportunity to use a noninvasive method for evaluating the teeth instead of using X-ray radiation for 2D X-ray images. Like food freshness analysis, pc-NIR LEDs for

bioimaging have not been extensively explored; however, initial results are genuinely encouraging.

5. CONCLUSIONS AND OUTLOOK

Despite significant advances in developing NIR light sources based on pc-LEDs, improvements are needed to advance this technology. Still, among all activator ions, Cr3+-substituted inorganic host crystal structures in a weak crystal field environment have the best potential to improve NIR commercial devices. This Spotlight on Applications highlights a set of design rules stemming from our work and work from leaders in the field that have enabled the creation of broadband Cr³⁺-substituted phosphors. We presented the current state of the art in Cr3+ literature from fundamental aspects to employment in pc-NIR LEDs. The key takeaways include guidelines for selecting host crystal structures that should produce broadband luminescence originating from the ⁴T₂ excited state. We also show how the crystal chemistry can be modified to obtain broadband emission, further broaden the fwhm, and red-shift the emission maximum toward the NIR region. Indeed, several strategies are available today following extensive research to create highly desirable NIR broadband emitters, including multisite occupancy of Cr3+, manipulating the energy of the crystal field splitting, or introducing structural disorders in the form of solid solutions. Besides broadband emission, parameters that should be considered when designing efficient Cr3+ phosphors are also highlighted. Indeed, the combination of high PLQY, low S parameter, high I_{423 K}, and broad fwhm can genuinely result in a highly efficient Cr3+ phosphor that could be used successfully in NIR LEDs applications. Initial research has successfully demonstrated the capability of applying Cr3+ pc-LEDS in fields such as night vision, food freshness testing, and in vitro imaging. As shown, Cr³⁺-substituted phosphors can be used to detect water or sugar in fruits and vegetables or to detect tissue damage in an easily accessible way. This field will continue to emerge as an active area for research and development, and based on the growing number of research papers in this field in the last year, it is likely that we will see continued progress in Cr³⁺ pc-NIR LEDs in the coming years.

AUTHOR INFORMATION

Corresponding Author

Jakoah Brgoch — Department of Chemistry, University of Houston, Houston, Texas 77204, United States; orcid.org/0000-0002-1406-1352; Email: jbrgoch@uh.edu

Authors

Małgorzata Sójka – Department of Chemistry, University of Houston, Houston, Texas 77204, United States; orcid.org/0000-0001-9346-8929

Jiyou Zhong — School of Physics and Optoelectronic Engineering, Guangdong University of Technology, Guangzhou 510006, China; ⊙ orcid.org/0000-0003-2817-6617

Complete contact information is available at: https://pubs.acs.org/10.1021/acsaom.3c00058

Notes

The authors declare no competing financial interest.

ACKNOWLEDGMENTS

The authors thank the National Science Foundation (DMR-1847701), the Guangzhou Basic and Applied Basic Research Project (202201010689), and Polish National Science Centre (NCN) under grant (#UMO-2020/37/N/ST5/02507).

REFERENCES

- (1) Benayas, A.; Hemmer, E.; Hong, G.; Jaque, D. Near Infrared-Emitting Nanoparticles for Biomedical Applications; Benayas, A.; Hemmer, E.; Hong, G.; Jaque, D., Eds.; Springer International Publishing: Cham, 2020. DOI: 10.1007/978-3-030-32036-2.
- (2) Chen, G.; Nie, W.; Zuo, J.; Li, Y.; Han, L.; Ye, X. A New Broadband Near-Infrared Emitting Mg₂Al₄Si₅O₁₈:Cr³⁺ Phosphor for Night-Vision Imaging. *Dalt. Trans.* **2022**, *51* (33), 12576–12584.
- (3) Liu, D.; Li, G.; Dang, P.; Zhang, Q.; Wei, Y.; Lian, H.; Shang, M.; Lin, C. C.; Lin, J. Simultaneous Broadening and Enhancement of Cr³⁺ Photoluminescence in LiIn₂SbO₆ by Chemical Unit Cosubstitution: Night-Vision and Near-Infrared Spectroscopy Detection Applications. *Angew. Chemie Int. Ed.* **2021**, *60* (26), 14644–14649.
- (4) Van Quang, N.; Thi Huyen, N.; Tu, N.; Quang Trung, D.; Duc Anh, D.; Tran, M. T.; Hung, N. D.; Viet, D. X.; Huy, P. T. A High Quantum Efficiency Plant Growth LED by Using a Deep-Red-Emitting α -Al₂O₃:Cr³⁺ phosphor. *Dalt. Trans.* **2021**, *S0* (36), 12570–12582.
- (5) Srivastava, A. M.; Brik, M. G.; Comanzo, H. A.; Beers, W. W.; Cohen, W. E.; Pocock, T. Spectroscopy of Mn⁴⁺ in Double Perovskites, La₂LiSbO₆ and La₂MgTiO₆: Deep Red Photon Generators for Agriculture LEDs. ECS J. Solid State Sci. Technol. **2018**, 7 (1), R3158–R3162.
- (6) Back, M.; Ueda, J.; Brik, M. G.; Tanabe, S. Pushing the Limit of Boltzmann Distribution in Cr³⁺-Doped CaHfO₃ for Cryogenic Thermometry. ACS Appl. Mater. Interfaces **2020**, 12 (34), 38325–38332.
- (7) Osborne, B. G. Near-Infrared Spectroscopy in Food Analysis. In *Encyclopedia of Analytical Chemistry*; John Wiley & Sons, Ltd: Chichester, UK, 2000; pp 1-14. DOI: 10.1002/9780470027318.a1018.
- (8) Beć, K. B.; Grabska, J.; Huck, C. W. Miniaturized NIR Spectroscopy in Food Analysis and Quality Control: Promises, Challenges, and Perspectives. *Foods* **2022**, *11* (10), 1465.
- (9) Fang, M. H.; Bao, Z.; Huang, W. T.; Liu, R. S. Evolutionary Generation of Phosphor Materials and Their Progress in Future Applications for Light-Emitting Diodes. *Chem. Rev.* **2022**, *122* (13), 11474–11513.
- (10) Hou, C. C.; Chen, H. M.; Zhang, J. C.; Zhuo, N.; Huang, Y. Q.; Hogg, R. A.; Childs, D. T. D.; Ning, J. Q.; Wang, Z. G.; Liu, F. Q.; Zhang, Z. Y. Near-Infrared and Mid-Infrared Semiconductor Broadband Light Emitters. *Light Sci. Appl.* **2018**, *7* (3), 17170.
- (11) Osram Datasheet: Oslon Black Flat, SFH 4735.
- (12) Bunzli, J.-C. G.; Piguet, C. Taking Advantage of Luminescent Lanthanide Ions. *Chem. Soc. Rev.* **2005**, 34 (12), 1048–1077.
- (13) Zhou, B.; Tao, L.; Tsang, Y. H.; Jin, W.; Pun, E. Y.-B. Superbroadband Near-IR Photoluminescence from Pr³⁺-Doped Fluorotellurite Glasses. *Opt. Express* **2012**, *20* (4), 3803.
- (14) Skripka, A.; Morinvil, A.; Matulionyte, M.; Cheng, T.; Vetrone, F. Advancing Neodymium Single-Band Nanothermometry. *Nanoscale* **2019**, *11* (23), 11322–11330.
- (15) van Swieten, T. P.; Yu, D.; Yu, T.; Vonk, S. J. W.; Suta, M.; Zhang, Q.; Meijerink, A.; Rabouw, F. T. A Ho³⁺-Based Luminescent Thermometer for Sensitive Sensing over a Wide Temperature Range. *Adv. Opt. Mater.* **2021**, 9 (1), 2001518.
- (16) Gavrilović, T. V.; Jovanović, D. J.; Lojpur, V.; Dramićanin, M. D. Multifunctional Eu³⁺- and Er³⁺/Yb³⁺-Doped GdVO₄ nanoparticles Synthesized by Reverse Micelle Method. *Sci. Rep.* **2014**, *4*, 1–9.
- (17) Blasse, G.; Grabbmaier, B. Luminescent Materials; Springer-Verlag Berlin Heidelberg, 1994.

- (18) Riseberg, L. A.; Moos, H. W. Multiphonon Orbit-Lattice Relaxation of Excited States of Rare-Earth Ions in Crystals. *Phys. Rev.* **1968**, *174* (2), 429–438.
- (19) Qin, X.; Liu, X.; Huang, W.; Bettinelli, M.; Liu, X. Lanthanide-Activated Phosphors Based on 4f-5d Optical Transitions: Theoretical and Experimental Aspects. *Chem. Rev.* **2017**, *117* (5), 4488–4527.
- (20) Berezovskaya, I. V.; Dotsenko, V. P.; Voloshinovskii, A. S.; Smola, S. S. Near Infrared Emission of Eu²⁺ Ions in Ca₃Sc₂Si₃O₁₂. *Chem. Phys. Lett.* **2013**, *585*, 11–14.
- (21) Qiao, J.; Zhou, G.; Zhou, Y.; Zhang, Q.; Xia, Z. Divalent Europium-Doped near-Infrared-Emitting Phosphor for Light-Emitting Diodes. *Nat. Commun.* **2019**, *10* (1), 1–7.
- (22) Zhu, Y.; Wang, X.; Qiao, J.; Molokeev, M. S.; Swart, H. C.; Ning, L.; Xia, Z. Regulating Eu²⁺ Multisite Occupation through Structural Disorder toward Broadband Near-Infrared Emission. *Chem. Mater.* **2023**, 35 (3), 1432–1439.
- (23) Lai, S.; Hu, T.; Molokeev, M. S.; Xia, Z. Photoluminescence Tuning in Ba₃ScB₃O₉:Eu²⁺ Phosphor by Crystal-Site Engineering. *Phys. Open* **2021**, 8 (June), 100077.
- (24) Yang, Z.; Zhao, Y.; Zhou, Y.; Qiao, J.; Chuang, Y.; Molokeev, M. S.; Xia, Z. Giant Red-Shifted Emission in (Sr,Ba)Y₂O₄:Eu²⁺ Phosphor Toward Broadband Near-Infrared Luminescence. *Adv. Funct. Mater.* **2022**, 32 (1), 2103927.
- (25) Wei, Y.; Gao, Z.; Yun, X.; Yang, H.; Liu, Y.; Li, G. Abnormal Bi^{3+} -Activated NIR Emission in Highly Symmetric $\mathrm{XAl}_{12}\mathrm{O}_{19}$ (X = Ba, Sr, Ca) by Selective Sites Occupation. *Chem. Mater.* **2020**, 32 (19), 8747–8753.
- (26) Song, E.; Jiang, X.; Zhou, Y.; Lin, Z.; Ye, S.; Xia, Z.; Zhang, Q. Heavy Mn²⁺ Doped MgAl₂O₄ Phosphor for High-Efficient Near-Infrared Light-Emitting Diode and the Night-Vision Application. *Adv. Opt. Mater.* **2019**, *7* (24), 1901105.
- (27) Du, J.; Poelman, D. Near-Infrared Persistent Luminescence in Mn⁴⁺ Doped Perovskite Type Solid Solutions. *Ceram. Int.* **2019**, 45 (7), 8345–8353.
- (28) Wang, J. Environmentally Friendly Fe³⁺-Activated near-Infrared-Emitting Phosphors for Spectroscopic Analysis. *Light Sci. Appl.* **2022**, *11* (1), 11–12.
- (29) Maiman, T. H. Stimulated Optical Radiation in Ruby. *Nature* **1960**, *187* (4736), 493–494.
- (30) Adachi, S. Review—Photoluminescence Properties of Cr³⁺-Activated Oxide Phosphors. *ECS J. Solid State Sci. Technol.* **2021**, *10* (2), 026001.
- (31) Rajendran, V.; Fang, M. H.; Guzman, G. N. De; Lesniewski, T.; Mahlik, S.; Grinberg, M.; Leniec, G.; Kaczmarek, S. M.; Lin, Y. S.; Lu, K. M.; Lin, C. M.; Chang, H.; Hu, S. F.; Liu, R. S. Super Broadband Near-Infrared Phosphors with High Radiant Flux as Future Light Sources for Spectroscopy Applications. *ACS Energy Lett.* **2018**, *3* (11), 2679–2684.
- (32) Zhong, J.; Zeng, L.; Zhao, W.; Brgoch, J. Producing Tunable Broadband Near-Infrared Emission through Co-Substitution in $(Ga_{1-x}Mg_x)(Ga_{1-x}Ge_x)O_3$:Cr³⁺. ACS Appl. Mater. Interfaces **2022**, 14, 51157.
- (33) Zhong, J.; Zhuo, Y.; Du, F.; Zhang, H.; Zhao, W.; Brgoch, J. Efficient and Tunable Luminescence in $Ga_{2-x}In_xO_3$: Cr^{3+} for Near-Infrared Imaging. ACS Appl. Mater. Interfaces **2021**, 13 (27), 31835—31842.
- (34) Zhong, J.; Li, C.; Zhao, W.; You, S.; Brgoch, J. Accessing High-Power Near-Infrared Spectroscopy Using Cr³⁺-Substituted Metal Phosphate Phosphors. *Chem. Mater.* **2022**, *34* (1), 337–344.
- (35) Zhong, J.; Zhuo, Y.; Du, F.; Zhang, H.; Zhao, W.; You, S.; Brgoch, J. Efficient Broadband Near-Infrared Emission in the GaTaO₄:Cr³⁺ Phosphor. *Adv. Opt. Mater.* **2022**, *10* (2), 2101800.
- (36) Liao, Z.; Li, C.; Zhong, J.; Li, Y.; Zhao, W. An Efficient and Thermally Stable Near-Infrared Phosphor Derives from Ln₃ScInGa₃O₁₂:Cr³⁺ (Ln = La, Gd, Y, and Lu) Garnet Family. *Dalt. Trans.* **2023**, *52*, 2853.
- (37) Dang, P.; Wei, Y.; Liu, D.; Li, G.; Lin, J. Recent Advances in Chromium-Doped Near-Infrared Luminescent Materials: Fundamen-

- tals, Optimization Strategies, and Applications. Adv. Opt. Mater. 2023, 11 (3), 2201739.
- (38) Zhao, F.; Song, Z.; Liu, Q. Advances in Chromium-Activated Phosphors for Near-Infrared Light Sources. *Laser Photon. Rev.* **2022**, *16* (11), 2200380.
- (39) De Guzman, G. N. A.; Fang, M. H.; Liang, C. H.; Bao, Z.; Hu, S. F.; Liu, R. S. Near-Infrared Phosphors and Their Full Potential: A Review on Practical Applications and Future Perspectives. *J. Lumin.* **2020**, 219, 116944.
- (40) Rajendran, V.; Chang, H.; Liu, R. S. Recent Progress on Broadband Near-Infrared Phosphors-Converted Light Emitting Diodes for Future Miniature Spectrometers. *Opt. Mater. X* **2019**, *1* (April), 100011.
- (41) Marciniak, L.; Bednarkiewicz, A.; Drabik, J.; Trejgis, K.; Strek, W. Optimization of Highly Sensitive YAG:Cr³⁺,Nd³⁺ Nanocrystal-Based Luminescent Thermometer Operating in an Optical Window of Biological Tissues. *Phys. Chem. Chem. Phys.* **2017**, *19* (10), 7343–7351.
- (42) Ueda, J.; Back, M.; Brik, M. G.; Zhuang, Y.; Grinberg, M.; Tanabe, S. Ratiometric Optical Thermometry Using Deep Red Luminescence from ⁴T₂ and ²E States of Cr³⁺ in ZnGa₂O₄ Host. *Opt. Mater. (Amst).* **2018**, *85*, 510–516.
- (43) You, L.; Tian, R.; Zhou, T.; Xie, R.-J. Broadband Near-Infrared Phosphor BaMgAl₁₀O₁₇:Cr³⁺ Realized by Crystallographic Site Engineering. *Chem. Eng. J.* **2021**, *417*, 129224.
- (44) Zeng, H.; Zhou, T.; Wang, L.; Xie, R. J. Two-Site Occupation for Exploring Ultra-Broadband Near-Infrared Phosphor Double-Perovskite La₂MgZrO₆:Cr³⁺. *Chem. Mater.* **2019**, 31 (14), 5245–5253.
- (45) Malysa, B.; Meijerink, A.; Jüstel, T. Temperature Dependent Cr^{3+} Photoluminescence in Garnets of the Type $X_3Sc_2Ga_3O_{12}$ (X = Lu, Y, Gd, La). *J. Lumin.* **2018**, 202 (May), 523–531.
- (46) Shannon, R. D. Revised Effective Ionic Radii and Systematic Studies of Interatomic Distances in Halides and Chalcogenides. *Acta Crystallogr., Sect. A* **1976**, *A*32, 751–767.
- (47) van Bunningen, A. J.; Sontakke, A. D.; Wakui, S.; Meijerink, A. Temperature Quenching of Cr^{3+} in $ASc(Si_{1-x}Ge_x)_2O_6$ (A = Li/Na) Solid Solutions. *Opt. Mater. (Amst).* **2022**, *128*, 112433.
- (48) Hariyani, S.; Brgoch, J. Luminescence in the Solid State. In Reference Module in Chemistry, Molecular Sciences and Chemical Engineering; Elsevier, 2022; pp 1–46. DOI: 10.1016/B978-0-12-823144-9.00067-4.
- (49) Brgoch, J.; Denbaars, S. P.; Seshadri, R. Proxies from Ab Initio Calculations for Screening Efficient Ce³⁺ Phosphor Hosts. *J. Phys. Chem. C* **2013**, *117* (35), 17955–17959.
- (50) Li, C.; Zhong, J. Highly Efficient Broadband Near-Infrared Luminescence with Zero-Thermal-Quenching in Garnet Y₃In₂Ga₃O₁₂:Cr³⁺ Phosphors. *Chem. Mater.* **2022**, 34 (18), 8418–8426.
- (51) Yang, Y.; Lu, Z.; Fan, H.; Chen, M.; Shen, L.; Zhang, X.; Pang, Q.; Chen, J.; Chen, P.; Zhou, L. Ultra-Broadband Near-Infrared Phosphors Realized by the Heterovalent Substitution Strategy. *Inorg. Chem.* **2023**, *62* (8), 3601–3608.
- (52) Zhang, H.; Li, C.; Zhong, J.; Wen, J.; Zhao, W. Thermally Robust Broadband Near-Infrared Luminescence in the NaGa-P₂O₇:Cr³⁺ Phosphor. *ACS Appl. Opt. Mater.* **2023**, *1* (1), 85–93.
- (53) Song, E.; Ming, H.; Zhou, Y.; He, F.; Wu, J.; Xia, Z.; Zhang, Q. Cr³⁺ -Doped Sc-Based Fluoride Enabling Highly Efficient Near Infrared Luminescence: A Case Study of K₂NaScF₆:Cr³⁺. *Laser Photon. Rev.* **2021**, *15* (2), 2000410.
- (54) Basore, E. T.; Xiao, W.; Liu, X.; Wu, J.; Qiu, J. Broadband Near-Infrared Garnet Phosphors with Near-Unity Internal Quantum Efficiency. *Adv. Opt. Mater.* **2020**, *8* (12), 2000296.
- (55) Zhang, H.; Zhong, J.; Du, F.; Chen, L.; Zhang, X.; Mu, Z.; Zhao, W. Efficient and Thermally Stable Broad-Band Near-Infrared Emission in a KAlP₂O₇:Cr³⁺ Phosphor for Nondestructive Examination. *ACS Appl. Mater. Interfaces* **2022**, *14* (9), 11663–11671.
- (56) Wu, Z.; Han, X.; Zhou, Y.; Xing, K.; Cao, S.; Chen, L.; Zeng, R.; Zhao, J.; Zou, B. Efficient Broadband Near-Infrared Luminescence

- of Cr³⁺ Doped Fluoride K₂NaInF₆ and Its NIR-LED Application toward Veins Imaging. *Chem. Eng. J.* **2022**, 427, 131740.
- (57) Jiang, H.; Chen, L.; Zheng, G.; Luo, Z.; Wu, X.; Liu, Z.; Li, R.; Liu, Y.; Sun, P.; Jiang, J. Ultra-Efficient GAGG:Cr³⁺ Ceramic Phosphor-Converted Laser Diode: A Promising High-Power Compact Near-Infrared Light Source Enabling Clear Imaging. *Adv. Opt. Mater.* **2022**, *10* (11), 2102741.
- (58) Huang, D.; Zhu, H.; Deng, Z.; Yang, H.; Hu, J.; Liang, S.; Chen, D.; Ma, E.; Guo, W. A Highly Efficient and Thermally Stable Broadband Cr³⁺ -Activated Double Borate Phosphor for near-Infrared Light-Emitting Diodes. *J. Mater. Chem. C* **2021**, *9* (1), 164–172.
- (59) Rajendran, V.; Fang, M.-H.; Huang, W.-T.; Majewska, N.; Lesniewski, T.; Mahlik, S.; Leniec, G.; Kaczmarek, S. M.; Pang, W. K.; Peterson, V. K.; Lu, K.-M.; Chang, H.; Liu, R.-S. Chromium Ion Pair Luminescence: A Strategy in Broadband Near-Infrared Light-Emitting Diode Design. J. Am. Chem. Soc. 2021, 143 (45), 19058–19066.
- (60) Lin, J.; Zhou, L.; Ren, L.; Shen, Y.; Chen, Y.; Fu, J.; Lei, L.; Ye, R.; Deng, D.; Xu, S. Broadband Near-Infrared Emitting Sr₃Sc4O₉:Cr³⁺ Phosphors: Luminescence Properties and Application in Light-Emitting Diodes. *J. Alloys Compd.* **2022**, *908*, 164582.
- (61) Mao, M.; Zhou, T.; Zeng, H.; Wang, L.; Huang, F.; Tang, X.; Xie, R. J. Broadband Near-Infrared (NIR) Emission Realized by the Crystal-Field Engineering of $Y_{3-x}Ca_xAl_{5-x}Si_xO_{12}$: Cr^{3+} (x=0-2.0) Garnet Phosphors. *J. Mater. Chem. C* **2020**, 8 (6), 1981–1988.
- (62) Yu, S.; Wei, Z.; Wu, J.; Wang, T.; Zhang, J.; Luo, X.; Li, Y.; Wang, C.; Zhao, L. Design and Tuning Cr³⁺-Doped near-Infrared Phosphors for Multifunctional Applications: Via Crystal Field Engineering. *Dalt. Trans.* **2022**, *51* (6), 2313–2322.
- (63) Hua, H.; Ueda, J.; Xu, J.; Back, M.; Tanabe, S. High-Pressure Photoluminescence Properties of Cr³⁺-Doped LaGaO₃ Perovskites Modulated by Pressure-Induced Phase Transition. *Inorg. Chem.* **2021**, 60 (24), 19253–19262.
- (64) Tran, M. T.; Trung, D. Q.; Tu, N.; Anh, D. D.; Thu, L. T. H.; Du, N. V.; Quang, N. V.; Huyen, N. T.; Kien, N. D. T.; Viet, D. X.; Hung, N. D.; Huy, P. T. Single-Phase Far-Red-Emitting ZnAl₂O₄:Cr³⁺ Phosphor for Application in Plant Growth LEDs. *J. Alloys Compd.* **2021**, 884, 161077.
- (65) Shi, Y.; Wang, Z.; Peng, J.; Wang, Y.; He, S.; Li, J.; Li, R.; Wei, G.; Yang, Y.; Li, P. Achieving the Ultra-Broadband near-Infrared La₃SnGa₅O₁₄:Cr³⁺ Phosphor via Multiple Lattice Sites Occupation for Biological Nondestructive Detection and Night-Vision Technology. *Mater. Today Adv.* **2022**, *16*, 100305.
- (66) Yu, H.; Chen, J.; Mi, R.; Yang, J.; Liu, Y. Broadband Near-Infrared Emission of K₃ScF₆:Cr³⁺ Phosphors for Night Vision Imaging System Sources. *Chem. Eng. J.* **2021**, *417* (March), 129271.
- (67) Lin, Q.; Wang, Q.; Liao, M.; Xiong, M.; Feng, X.; Zhang, X.; Dong, H.; Zhu, D.; Wu, F.; Mu, Z. Trivalent Chromium Ions Doped Fluorides with Both Broad Emission Bandwidth and Excellent Luminescence Thermal Stability. ACS Appl. Mater. Interfaces 2021, 13 (15), 18274–18282.
- (68) Jia, Z.; Yuan, C.; Liu, Y.; et al. Strategies to Approach High Performance in Cr³⁺ -Doped Phosphors for High-Power NIR-LED Light Sources. *Light Sci. Appl.* **2020**, *9*, 86.
- (69) Wang, C.; Wang, X.; Zhou, Y.; Zhang, S.; Li, C.; Hu, D.; Xu, L.; Jiao, H. An Ultra-Broadband Near-Infrared Cr³⁺-Activated Gallogermanate Mg₃Ga₂GeO₈ Phosphor as Light Sources for Food Analysis. ACS Appl. Electron. Mater. **2019**, *1* (6), 1046–1053.
- (70) Yu, H.; Yang, J.; Liu, Y.; Xie, C.; Huang, Z.; Mei, L. Green HF-Free Synthetic Route to the High-Efficiency K_2NaGaF_6 : Cr^{3+} Phosphor and Its NIR-LED Application toward Veins Imaging. ACS Sustain. Chem. Eng. **2022**, 10 (24), 8022–8030.
- (71) Fang, M.; Huang, P.; Bao, Z.; Majewska, N.; Leśniewski, T.; Mahlik, S.; Grinberg, M.; Leniec, G.; Kaczmarek, S. M.; Yang, C.-W.; Lu, K.-M.; Sheu, H.; Liu, R. Penetrating Biological Tissue Using Light-Emitting Diodes with a Highly Efficient Near-Infrared ScBO₃:Cr³⁺ Phosphor. *Chem. Mater.* **2020**, 32 (5), 2166–2171.
- (72) Lu, C. H.; Tsai, Y. T.; Tsai, T. L.; Chan, T. S.; Zhang, X.; Lin, C. C. Cr³⁺-Sphere Effect on the Whitlockite-Type NIR Phosphor

 $Sr_9Sc(PO_4)_7$ with High Heat Dissipation for Digital Medical Applications. *Inorg. Chem.* **2022**, *61* (5), 2530–2537.